

## Experimental and Theoretical Studies of the Site Occupancy and Luminescence of Ce<sup>3+</sup> in LiSr<sub>4</sub>(BO<sub>3</sub>)<sub>3</sub> for Potential X-ray Detecting Applications

Yang, Yunlin; Lou, Bibo; Ou, Yiyi; Su, Fang; Ma, Chong Geng; Duan, Chang Kui; Dorenbos, Pieter; Liang, Hongbin

**DOI**

[10.1021/acs.inorgchem.2c01016](https://doi.org/10.1021/acs.inorgchem.2c01016)

**Publication date**

2022

**Document Version**

Final published version

**Published in**

Inorganic Chemistry

**Citation (APA)**

Yang, Y., Lou, B., Ou, Y., Su, F., Ma, C. G., Duan, C. K., Dorenbos, P., & Liang, H. (2022). Experimental and Theoretical Studies of the Site Occupancy and Luminescence of Ce<sup>3+</sup> in LiSr<sub>4</sub>(BO<sub>3</sub>)<sub>3</sub> for Potential X-ray Detecting Applications. *Inorganic Chemistry*, 61(19), 7654-7662. <https://doi.org/10.1021/acs.inorgchem.2c01016>

**Important note**

To cite this publication, please use the final published version (if applicable). Please check the document version above.

**Copyright**

Other than for strictly personal use, it is not permitted to download, forward or distribute the text or part of it, without the consent of the author(s) and/or copyright holder(s), unless the work is under an open content license such as Creative Commons.

**Takedown policy**

Please contact us and provide details if you believe this document breaches copyrights. We will remove access to the work immediately and investigate your claim.

***Green Open Access added to TU Delft Institutional Repository***

***'You share, we take care!' - Taverne project***

**<https://www.openaccess.nl/en/you-share-we-take-care>**

Otherwise as indicated in the copyright section: the publisher is the copyright holder of this work and the author uses the Dutch legislation to make this work public.

# Experimental and Theoretical Studies of the Site Occupancy and Luminescence of Ce<sup>3+</sup> in LiSr<sub>4</sub>(BO<sub>3</sub>)<sub>3</sub> for Potential X-ray Detecting Applications

Yunlin Yang, Bibo Lou, Yiyi Ou, Fang Su, Chong-Geng Ma, Chang-Kui Duan, Pieter Dorenbos, and Hongbin Liang\*



Cite This: *Inorg. Chem.* 2022, 61, 7654–7662



Read Online

ACCESS |



Metrics & More

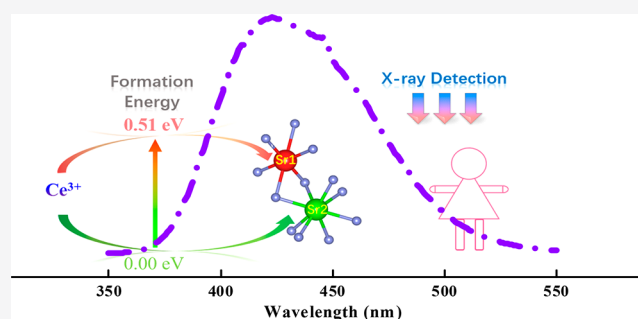


Article Recommendations



Supporting Information

**ABSTRACT:** Ce<sup>3+</sup>-doped LiSr<sub>4</sub>(BO<sub>3</sub>)<sub>3</sub> phosphors have been prepared by a high-temperature solid-state reaction method, and structural refinement of the host compound has been performed. The excitation and emission spectra in the vacuum ultraviolet–ultraviolet–visible range at cryogenic temperatures reveal that Ce<sup>3+</sup> ions preferentially occupy eight-coordinated Sr<sup>2+</sup> sites in LiSr<sub>4</sub>(BO<sub>3</sub>)<sub>3</sub>. Such experimental attribution is well corroborated by the calculated 4f–5d transition energies and defect formation energies of Ce<sup>3+</sup> ions at two distinct Sr<sup>2+</sup> sites in the first-principles framework. In addition, the doping concentration-dependent luminescence and the temperature-dependent luminescence are systematically investigated by luminescence intensity and lifetime measurements, respectively. This shows that concentration quenching does not occur in the investigated doping range, but inhomogeneous broadening exists in the concentrated samples. With the estimated thermal quenching activation energy, the discussions on the thermal quenching mechanisms suggest that the thermal-ionization process of the 5d electron is a dominant channel for thermal quenching of Ce<sup>3+</sup> luminescence, despite the fact that thermally activated concentration quenching cannot be excluded for the highly doped samples. Finally, the X-ray excited luminescence measurement demonstrates the promising applications of the phosphors in X-ray detection.



## 1. INTRODUCTION

The investigation of the luminescence of Ce<sup>3+</sup> in various host compounds has always been a fascinating field because of its fundamental significance and wide application.<sup>1,2</sup> From the viewpoint of basic research, the Ce<sup>3+</sup> ion shows typical 4f–5d transitions. Due to the simplest 4f<sup>1</sup> and 5d<sup>1</sup> electronic configurations of a Ce<sup>3+</sup> ion in the ground and excited states, the energies of f–d transitions of Ce<sup>3+</sup> in a host compound can provide a key reference to those of lanthanide ions such as Eu<sup>2+</sup> and Pr<sup>3+</sup> in the same lattice sites of the same host compounds.<sup>3</sup> In addition, the luminescence of Ce<sup>3+</sup> is also important for actual applications, and Ce<sup>3+</sup>-doped materials have been utilized in different fields after years of continuous efforts. For example, Y<sub>3</sub>Al<sub>5</sub>O<sub>12</sub>:Ce<sup>3+</sup> is well-known as a yellow-emitting phosphor in phosphor-converted light-emitting diodes (pc-LEDs). The scintillators Lu<sub>2</sub>SiO<sub>5</sub>:Ce<sup>3+</sup>, LuAlO<sub>3</sub>:Ce<sup>3+</sup>, and LnX<sub>3</sub>:Ce<sup>3+</sup> (Ln = La, and X = Cl or Br; Ln = Lu, and X = I) have been used commercially to detect ionizing radiation.<sup>1,4</sup>

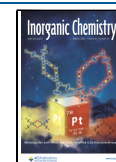
Because the crystal field strength has a strong influence on the outer 5d orbital of Ce<sup>3+</sup>, the 4f–5d transition energies of Ce<sup>3+</sup> may present remarkable variations in different coordination surroundings. Such a structural factor, which is controlled

by site occupancy, directly governs the various aspects of the luminescence properties.<sup>5–7</sup> Apparently, a clear understanding of the site occupancy of Ce<sup>3+</sup> in the host compound is crucial for the development of novel lanthanide ion-doped luminescent materials with f–d transitions. To the best of our knowledge, a systematic analysis of the crystal field splitting (CFS) and centroid of Ce<sup>3+</sup> 5d energy levels is a good approach for gaining insight into the site occupancies of the doping Ce<sup>3+</sup> ions experimentally.<sup>8,9</sup> Furthermore, the first-principles calculations of the energies of f–d transitions corroborate the site occupancies, and those on the formation and transition energies of Ce<sup>3+</sup> ions in different sites give an explanation for the preferential occupancies theoretically.<sup>10,11</sup>

LiSr<sub>4</sub>(BO<sub>3</sub>)<sub>3</sub> is an efficient host compound for luminescence of lanthanide ions, which has two Sr<sup>2+</sup> sites in six- and eight-

Received: March 28, 2022

Published: May 5, 2022



fold coordination, respectively.<sup>12</sup> In this paper, the vacuum ultraviolet–ultraviolet–visible (VUV–UV–vis) spectra of Ce<sup>3+</sup>-doped LiSr<sub>4</sub>(BO<sub>3</sub>)<sub>3</sub> are first investigated at cryogenic temperatures in detail to understand the bandgap of the host compound, the site occupancy, and the 4f–5d transition energies of Ce<sup>3+</sup> in this site experimentally. Then the first-principles calculations on the f–d transition energies and the formation and transition energies of Ce<sup>3+</sup> ions in different sites confirm and explain the preferential site occupations theoretically. In addition, the concentration- and temperature-dependent luminescence characteristics are discussed in terms of the luminescence intensity and lifetime, respectively. The possible application of the phosphor for X-ray detection is demonstrated. This work provides a systematic method for understanding the preferential site occupancies through a combination of experiments and theoretical calculations. It is conducive to the design of novel luminescent materials.

## 2. METHODOLOGY

**2.1. Experimental Details.** A series of Li<sub>1+x</sub>Sr<sub>4-2x</sub>Ce<sub>x</sub>(BO<sub>3</sub>)<sub>3</sub> ( $x = 0, 0.001, 0.005, 0.01, \text{ or } 0.03$ ) samples were prepared by a traditional high-temperature solid-state reaction method using Li<sub>2</sub>CO<sub>3</sub> [analytical reagent (A.R.)], SrCO<sub>3</sub> (A.R.), CeO<sub>2</sub> (99.99%), and H<sub>3</sub>BO<sub>3</sub> (A.R.) as raw materials. After stoichiometrically weighed, thoroughly mixed, and ground, all reactants were transferred to the crucibles and sintered in a muffle furnace at 850 °C for 8 h in a N<sub>2</sub>–H<sub>2</sub> reducing gas ambience. When the product cooled to room temperature (RT) naturally, it was ground for subsequent characterizations.

The phase purity and crystal structure of typical samples were characterized by powder X-ray diffraction (XRD) measurements on a Bruker D8 ADVANCE instrument with Cu K $\alpha$  radiation ( $\lambda = 1.5418$  Å) at 35 kV and 35 mA. The data were collected over a  $2\theta$  range from 10° to 80° with a scanning speed of 10°/min. The high-quality XRD data for structural Rietveld refinements were recorded over a  $2\theta$  range from 10° to 100° with an interval of 0.02°, and the refinements were performed by using TOPAS Academic software.<sup>13</sup> The VUV–UV–vis excitation and emission spectra were recorded on beamline 4B8 of the Beijing Synchrotron Radiation Facility (BSRF) under normal operating conditions by using the spectrum of sodium salicylate (*o*-C<sub>6</sub>H<sub>4</sub>OHCOONa) as a reference. The UV–vis emission and excitation spectra as well as the luminescence decay curves were recorded on an Edinburgh FLS1000 spectrometer. A 450 W Xe lamp was used as the excitation source for steady-state spectra, and a light-emitting diode laser with a pulse width of 736.7 ps and a pulse repetition rate of 2000 kHz was used for luminescence decay measurements. A model PET 980 detector was used to accept the signal. The temperature-variable spectroscopy test was carried out using an Oxford model Optistat DN cryostat and controlled by a Mercury model iTC temperature controller. The X-ray excitation luminescence (XEL) measurement was carried out on a Philips PW2253/20 X-ray tube at Delft University of Technology.<sup>14</sup>

**2.2. Computational Details.** To better understand the origin of the measured excitation and emission spectra, we performed first-principles calculations on the formation energies and transition energies of Ce<sup>3+</sup> at two different Sr<sup>2+</sup> sites in LiSr<sub>4</sub>(BO<sub>3</sub>)<sub>3</sub>. One of the Sr<sup>2+</sup> ions in the 1 × 1 × 1 supercell containing 272 atoms was replaced with Ce<sup>3+</sup>, and structural optimization was carried out under the framework of density functional theory (DFT) utilizing the Perdew–Burke–Ernzerof exchange–correlation functional.<sup>15</sup> A Hubbard *U* of 2.5 eV was adopted for the 4f orbitals of the Ce ion. To improve the description of bandgaps and Ce<sup>3+</sup>-related energy levels, a modified PBE0 with 31% Hartree–Fock exchange was determined by the inverse of the calculated value of the optical dielectric constant, 1/ $\epsilon_{\infty}$ . By applying the constrained occupancy method, we obtained the equilibrium structure of the lowest excited state of LiSr<sub>4</sub>(BO<sub>3</sub>)<sub>3</sub>:Ce<sup>3+</sup> in which one electron on the 4f Kohn–Sham (KS) orbital was excited to the lowest 5d KS orbital. Thermodynamic charge transition level  $\epsilon(\text{Ce}^{3+/4+})$  is defined as the electron Fermi level to equate the

formation energies of Ce<sup>3+</sup> and Ce<sup>4+</sup> dopants calculated at their corresponding equilibrium supercells. Relative to the valence band maximum (VBM),  $\epsilon(\text{Ce}^{3+/4+}) = E_{\text{tot}}(\text{Ce}^{3+}) - E_{\text{tot}}(\text{Ce}^{4+}) - \epsilon_{\text{VBM}}$ , where  $E_{\text{tot}}$  is the total energy of the relaxed structure of the LiSr<sub>4</sub>(BO<sub>3</sub>)<sub>3</sub> supercell containing Ce<sup>3+</sup> or Ce<sup>4+</sup> and  $\epsilon_{\text{VBM}}$  is the position of the valence band maximum obtained by employing modified PBE0 with a Hatree–Fock mixing parameter  $\alpha$  of 0.31. The 4f–5d excitation energies were obtained from the differences in the generalized KS eigenvalues calculated at the equilibrium geometric structure of the Ce<sup>3+</sup> supercell. More details about the calculation procedures and their justifications can be found in ref 16 and are not elaborated here. The relative formation energies of Ce<sup>3+</sup> between two sites are calculated with 4f-in-core pseudopotentials, and their relative concentration was estimated by the term  $\omega \exp(-\Delta E_f/k_B T)$ , where  $\omega$ ,  $\Delta E_f$ ,  $k_B$ , and  $T$  are the ratio of sites to be occupied, the difference in formation energy, the Boltzmann constant, and the temperature of sample preparation, respectively.

## 3. RESULTS AND DISCUSSION

**3.1. X-ray Diffraction (XRD), Structural Refinement, and Crystal Structure.** To verify the phase purity and check the crystal structure, the high-quality XRD pattern of the host compound LiSr<sub>4</sub>(BO<sub>3</sub>)<sub>3</sub> was collected and the Rietveld refinement was carried out by using the cubic structure as the original model as shown in Figure 1a. The values of  $R_{\text{wp}}$

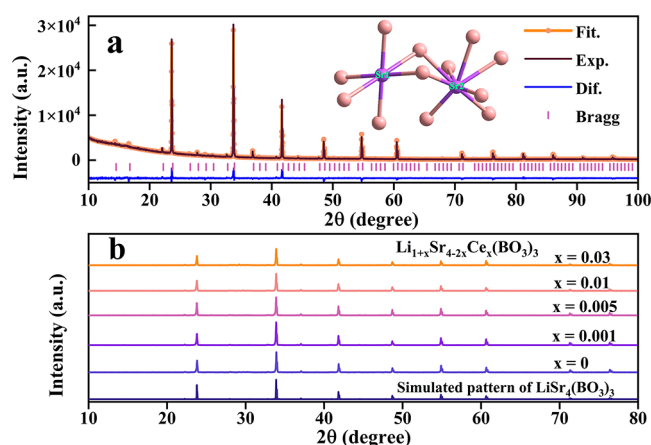


**Figure 1.** (a) Rietveld refinement result of XRD data of the LiSr<sub>4</sub>(BO<sub>3</sub>)<sub>3</sub> compound at RT. The orange-point line represents the fitting curve, the black line the experimental data, and the blue line the difference between the experimental data and fitting curve, and the purple bars are the Bragg positions. The inset shows the schematic coordination surroundings of two Sr<sup>2+</sup> sites in the host lattice. (b) Concentration-dependent XRD patterns of Li<sub>1+x</sub>Sr<sub>4-2x</sub>Ce<sub>x</sub>(BO<sub>3</sub>)<sub>3</sub> ( $x = 0, 0.001, 0.005, 0.01, \text{ or } 0.03$ ). The bottom simulated pattern of LiSr<sub>4</sub>(BO<sub>3</sub>)<sub>3</sub> was calculated by the VESTA program based on its Crystallographic Information Framework (CIF) file.<sup>17</sup>

( $\sim 5.98\%$ ),  $R_p$  ( $\sim 3.91\%$ ), and  $R_B$  ( $\sim 7.87\%$ ) all mean a fine fitting result, implying reliable refined indicators for proving LiSr<sub>4</sub>(BO<sub>3</sub>)<sub>3</sub> was free of impurities. The refined lattice parameters are as follows:  $a = b = c = 14.949$  Å,  $V = 3340.484$  Å<sup>3</sup>, and  $Z = 16$ . The detailed structural parameters are listed in Table 1. The compound LiSr<sub>4</sub>(BO<sub>3</sub>)<sub>3</sub> crystallizes in a cubic structure with space group *Ia* $\bar{3}d$ , in which Sr<sup>2+</sup> ions occupy two diverse lattice sites.<sup>12</sup> The schematic coordination surroundings of these two Sr<sup>2+</sup> ions are shown as insets in the top right corner of Figure 1a. Sr<sup>2+</sup>(1) ions are six-fold coordinated to form distorted octahedral [Sr(1)O<sub>6</sub>] at the 16a Wyckoff position with S<sub>6</sub> symmetry, while Sr<sup>2+</sup>(2) ions are eight-fold coordinated in two-capped trigonal prisms

**Table 1.** Refined Structural Parameters of  $\text{LiSr}_4(\text{BO}_3)_3$  at Room Temperature

atom	Wyckoff position	x	y	z	occupation	$B_{\text{eq}}$
Sr1	16a	0	0	0	1	1.48
Sr2	48f	0	0.25	-0.001	1	0.84
Li	16b	0.125	0.125	0.125	1	1.60
B	96h	0.163	0.352	0.125	1	0.24
O1	96h	-0.020	0.272	0.041	1	0.55
O2	96h	0.264	0.365	0.125	1	1.89

$[\text{Sr}(2)\text{O}_8]$  at the 48f Wyckoff position with  $C_2$  symmetry. The average Sr–O bond distances for  $[\text{Sr}(1)\text{O}_6]$  and  $[\text{Sr}(2)\text{O}_8]$  polyhedra are 2.536 and 2.630 Å, respectively. The nearest  $\text{Sr}^{2+}(1)$ – $\text{Sr}^{2+}(1)$ ,  $\text{Sr}^{2+}(2)$ – $\text{Sr}^{2+}(2)$ , and  $\text{Sr}^{2+}(1)$ – $\text{Sr}^{2+}(2)$  distances are approximately 6.474, 3.665, and 3.738 Å, respectively.

The XRD patterns of  $\text{Ce}^{3+}$ -doped  $\text{Li}_{1+x}\text{Sr}_{4-2x}\text{Ce}_x(\text{BO}_3)_3$  ( $x = 0, 0.001, 0.005, 0.01, \text{ or } 0.03$ ) samples were further measured as presented in Figure 1b. Since the standard XRD card of  $\text{LiSr}_4(\text{BO}_3)_3$  was not found in the powder diffraction files (PDF) database, the simulated pattern of  $\text{LiSr}_4(\text{BO}_3)_3$  at the bottom of the graph was obtained using VESTA program according to its CIF file.<sup>17</sup> For the samples with different doping contents, their XRD patterns are identical to the simulated one and all diffraction peaks can be indexed to the simulated pattern, indicating that these  $\text{Ce}^{3+}$ -doped samples are without impurities; this can be further confirmed by the luminescence spectra in section 3.2. In addition, the observations imply that the doping  $\text{Ce}^{3+}$  ions do not clearly affect the crystal structure of the  $\text{LiSr}_4(\text{BO}_3)_3$  host. Considering the similar ionic radii of  $\text{Ce}^{3+}$  and  $\text{Sr}^{2+}$  [for a coordination number (CN) of 6,  $r(\text{Ce}^{3+}) = 1.01$  Å and  $r(\text{Sr}^{2+}) = 1.18$  Å; for a CN of 8,  $r(\text{Ce}^{3+}) = 1.14$  Å and  $r(\text{Sr}^{2+}) = 1.26$  Å],<sup>18</sup>  $\text{Ce}^{3+}$  ions are assumed to enter  $\text{Sr}^{2+}$  sites. In sections 3.2–3.3, we will discuss the site occupancy through experimental luminescence spectra and theoretical calculations in detail.

**3.2. Excitation and Emission Wavelength Dependencies of the Luminescence of  $\text{Li}_{1.001}\text{Sr}_{3.998}\text{Ce}_{0.001}(\text{BO}_3)_3$ .** Figure 2a displays the highest height-normalized excitation ( $\lambda_{\text{em}} = 390, 400, 418, 420, 450, 470, \text{ and } 485$  nm) and emission ( $\lambda_{\text{ex}} = 268, 286, \text{ and } 332$  nm) spectra of the  $\text{Li}_{1.001}\text{Sr}_{3.998}\text{Ce}_{0.001}(\text{BO}_3)_3$  sample at RT for comparison. Herein, wavelengths of 268, 286, and 332 nm are close to the peaks of three bands in the excitation spectra, and wavelengths of 390, 400, 418, 420, 450, 470, and 485 nm are near 35%, 65%, 100%, 100%, 80%, 55%, and 30% of the emission peak, respectively. Under varied wavelength excitation, three emission curves almost overlap with one another. Meanwhile, seven normalized excitation spectra also nearly overlap by monitoring the selected emission wavelengths. The observations suggest that the sample does not contain any impurity that affects the luminescence in this spectral range, and  $\text{Ce}^{3+}$  ions occupy only one kind of site in this sample.

Upon 320 nm excitation, the luminescence decay curves of  $\text{Li}_{1.001}\text{Sr}_{3.998}\text{Ce}_{0.001}(\text{BO}_3)_3$  of different wavelength emission are shown in Figure 2b. All curves overlap, and the luminescence lifetime of  $\text{Li}_{1.001}\text{Sr}_{3.998}\text{Ce}_{0.001}(\text{BO}_3)_3$  is exponentially fitted to be approximately  $\sim 41.3$  ns at 78 K. The observation further illustrates the existence of only a single kind of  $\text{Ce}^{3+}$  luminescence center in the host compound, and the

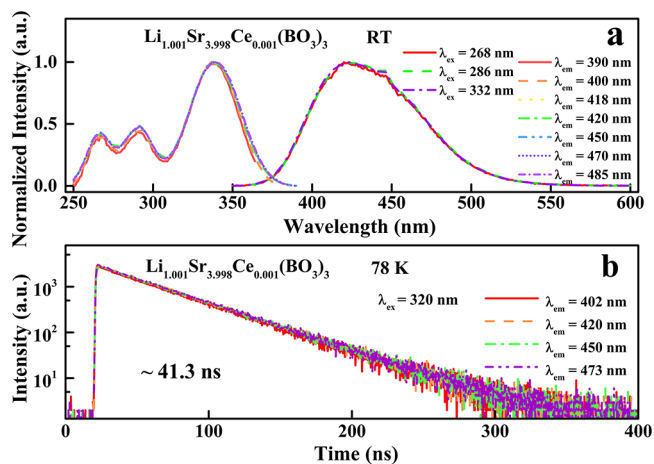


**Figure 2.** (a) Highest height-normalized excitation ( $\lambda_{\text{em}} = 390, 400, 418, 420, 450, 470, \text{ and } 485$  nm) and emission ( $\lambda_{\text{ex}} = 268, 286, \text{ and } 332$  nm) spectra of the  $\text{Li}_{1.001}\text{Sr}_{3.998}\text{Ce}_{0.001}(\text{BO}_3)_3$  sample at room temperature. (b) Luminescence decay curves ( $\lambda_{\text{ex}} = 320$  nm, and  $\lambda_{\text{em}} = 402, 420, 450, \text{ and } 473$  nm) of the  $\text{Li}_{1.001}\text{Sr}_{3.998}\text{Ce}_{0.001}(\text{BO}_3)_3$  sample at 78 K.

inhomogeneous broadening effect is not pronounced in this diluted  $\text{Li}_{1.001}\text{Sr}_{3.998}\text{Ce}_{0.001}(\text{BO}_3)_3$  sample.<sup>19</sup>

**3.3. VUV–UV–vis Luminescence of  $\text{Li}_{1.001}\text{Sr}_{3.998}\text{Ce}_{0.001}(\text{BO}_3)_3$  at Cryogenic Temperatures and Site Occupancy of  $\text{Ce}^{3+}$ .** To clarify the site occupancy and the 5d energies of  $\text{Ce}^{3+}$  in this host compound, the VUV–UV–vis luminescence spectra of  $\text{Li}_{1.001}\text{Sr}_{3.998}\text{Ce}_{0.001}(\text{BO}_3)_3$  are recorded at cryogenic temperatures. The purple line in Figure 3a presents the UV excitation ( $\lambda_{\text{em}} = 420$  nm) spectrum of this

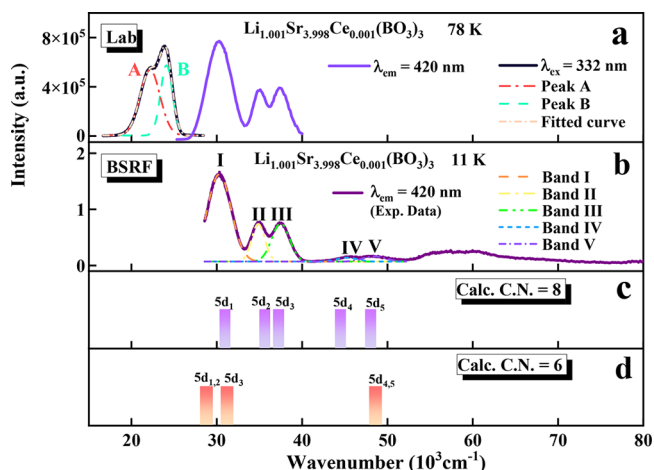


**Figure 3.** (a) Lab UV excitation ( $\lambda_{\text{em}} = 420$  nm) and UV–vis emission ( $\lambda_{\text{ex}} = 332$  nm) spectra of  $\text{Li}_{1.001}\text{Sr}_{3.998}\text{Ce}_{0.001}(\text{BO}_3)_3$  at 78 K. (b) Synchrotron radiation VUV–UV excitation spectrum ( $\lambda_{\text{em}} = 420$  nm) of  $\text{Li}_{1.001}\text{Sr}_{3.998}\text{Ce}_{0.001}(\text{BO}_3)_3$  at 11 K. (c and d) Calculated 4f–5d<sub>j</sub> ( $j = 1$ –5) transition energies of  $\text{Ce}^{3+}$  ions in two  $\text{Sr}^{2+}$  sites of  $\text{LiSr}_4(\text{BO}_3)_3$ .

sample using an Edinburgh FLS1000 spectrometer at 78 K. Three distinct broad bands are seen with maxima at  $\sim 30.2 \times 10^3 \text{ cm}^{-1}$  (331 nm, 3.74 eV),  $\sim 35.0 \times 10^3 \text{ cm}^{-1}$  (286 nm, 4.33 eV), and  $\sim 37.4 \times 10^3 \text{ cm}^{-1}$  (267 nm, 4.64 eV). The lowest 4f–5d excitation band of  $\text{Ce}^{3+}$  in  $\text{LiSr}_4(\text{BO}_3)_3$  has been reported around the range of 340–356 nm, which are largely in agreement with the value observed in Figure 3a.<sup>20–22</sup> The

deviation may be the result of different measurement instruments, temperatures, etc.

The black line in Figure 3a shows the emission spectrum of  $\text{Li}_{1.001}\text{Sr}_{3.998}\text{Ce}_{0.001}(\text{BO}_3)_3$  upon 332 nm excitation at 78 K. The band position is consistent with that in Figure 2a, but the spectral resolution is better due to the low-temperature condition. It consists of a main band and a shoulder band at the shorter wavenumber side. The spectrum can be well-fitted with a sum of two Gaussian functions. Accordingly, two band peaks are estimated at  $\sim 22.2 \times 10^3 \text{ cm}^{-1}$  (peak A, 450 nm, 2.75 eV) and  $\sim 24.1 \times 10^3 \text{ cm}^{-1}$  (peak B, 415 nm, 2.99 eV). Their energy separation ( $\sim 1.90 \times 10^3 \text{ cm}^{-1}$ , 0.24 eV) corresponds to typical values of  ${}^2\text{F}_{5/2}$  and  ${}^2\text{F}_{7/2}$  spin-orbit split 4f ground states of  $\text{Ce}^{3+}$ . From the energy difference between the band maxima of the  ${}^2\text{F}_{5/2}$ – $5d_1$  transition in excitation (3.74 eV) and emission (2.99 eV) spectra, the Stokes shift of  $\text{Ce}^{3+}$  in  $\text{LiSr}_4(\text{BO}_3)_3$  is evaluated to be 0.75 eV, indicating that the 5d electrons of  $\text{Ce}^{3+}$  in  $\text{LiSr}_4(\text{BO}_3)_3$  experience a strong effect of electron–phonon interaction with the coordination environment.<sup>3</sup>

Figure 3b exhibits the synchrotron radiation VUV–UV excitation ( $\lambda_{\text{em}} = 420 \text{ nm}$ ) spectrum of  $\text{Li}_{1.001}\text{Sr}_{3.998}\text{Ce}_{0.001}(\text{BO}_3)_3$  recorded on beamline 4B8 of the Beijing Synchrotron Radiation Facility (BSRF) at 11 K. The whole excitation profile includes the host-related absorption with an energy above  $\sim 52.2 \times 10^3 \text{ cm}^{-1}$  and the 4f–5d transitions of  $\text{Ce}^{3+}$  ions below this wavenumber. First, the bandgap of host compound  $\text{LiSr}_4(\text{BO}_3)_3$  is evaluated according to the spectrum in Figure 3b. The host exciton creation energy ( $E^{\text{ex}}$ ) is found to be  $\sim 56.8 \times 10^3 \text{ cm}^{-1}$  ( $\sim 7.04 \text{ eV}$ , 176 nm). This assignment can be further confirmed by the synchrotron radiation VUV–UV excitation spectrum of the  $\text{Li}_{1.001}\text{Sr}_{3.998}\text{Gd}_{0.001}(\text{BO}_3)_3$  sample in Figure S1, in which an evident excitonic absorption band with a maximum at  $\sim 175 \text{ nm}$  can be observed when the 312 nm emission of the  $\text{Gd}^{3+} {}^6\text{P}_{7/2} \rightarrow {}^8\text{S}_{7/2}$  transition is monitored. In addition, a conspicuous host-related band has been observed near  $\sim 7 \text{ eV}$  of isomorphous compound  $\text{NaSr}_4(\text{BO}_3)_3$ .<sup>23</sup> Considering the electron transfer from the upper valence band to the conduction band bottom, the optical bandgap value of the host compound should add the electron–hole binding energy of an exciton to the host exciton creation absorption energy ( $E^{\text{ex}}$ ). The binding energy can be estimated to be  $0.008 \times (E^{\text{ex}})^{2.24}$ . In our case, upon addition of the electron–hole binding energy to the exciton creation energy, the bandgap energy of the  $\text{LiSr}_4(\text{BO}_3)_3$  compound between the upper valence band and conduction band bottom is calculated to be  $\sim 7.44 \text{ eV}$ .

Then, we discuss the 4f–5d excitation bands of  $\text{Ce}^{3+}$  ions in Figure 3b. As mentioned in section 3.2,  $\text{Ce}^{3+}$  ions enter only one type of  $\text{Sr}^{2+}$  site in  $\text{LiSr}_4(\text{BO}_3)_3$ . Hence, at most five 4f–5d transition bands might occur in the excitation spectrum. This is exactly what we find in the range of  $28.6 \times 10^3$  to  $52.2 \times 10^3 \text{ cm}^{-1}$  of the spectrum at 11 K, which contains a strong band (I), two medium bands (II and III), and two very weak overlapping bands. The positions and profiles of three obvious low-energy bands (I–III) are consistent with those in Figure 3a. To better evaluate these excitation peaks, a sum of five Gaussian functions is adopted to fit the curve at this range. The peak maxima of these bands are estimated to be  $\sim 30.2 \times 10^3 \text{ cm}^{-1}$  (band I, 3.74 eV, 331 nm),  $\sim 34.9 \times 10^3 \text{ cm}^{-1}$  (band II, 4.33 eV, 286 nm),  $\sim 37.5 \times 10^3 \text{ cm}^{-1}$  (band III, 4.64 eV, 267 nm),  $\sim 45.2 \times 10^3 \text{ cm}^{-1}$  (band IV, 5.61 eV, 221 nm), and

$\sim 48.5 \times 10^3 \text{ cm}^{-1}$  (band V, 6.01 eV, 206 nm), which are attributed to the  $\text{Ce}^{3+}$  transitions from the 4f ground state to the first to fifth 5d ( $5d_{1-5}$ ) excitation states, respectively. The different intensity distributions of five excitation bands may relate to the energy separation between the conduction band minimum (CBM) and the  $5d_{1-5}$  multiplets as shown in Figure 7 (vide infra).  $5d_1$  is fairly below the CBM in energy, so the 4f– $5d_1$  excitation band is strong; the  $5d_{2,3}$  energy levels are close to the CBM. Hence, the 4f– $5d_{2,3}$  excitation bands are with medium intensities, but the  $5d_{4,5}$  levels are evidently higher than the CBM; therefore, the 4f– $5d_{4,5}$  excitation bands are very weak due to autoionization processes.<sup>3</sup>

Herein, the centroid energy of  $\text{Ce}^{3+}$  ion 5d states in  $\text{LiSr}_4(\text{BO}_3)_3$  is estimated to be  $\sim 4.87 \text{ eV}$  by calculating the arithmetic average energy of five 4f–5d excitation bands, which is larger than that of borate  $\text{LiCaBO}_3$  [4.46 eV,  $C_1$  point symmetry ( $\text{CaO}_7$ ) polyhedron with a mean bond length of 2.428 Å], close to that of  $\text{LaBO}_3$  [4.92 eV,  $C_s$  point symmetry ( $\text{LaO}_9$ ) polyhedron with an average bond distance of 2.602 Å], but smaller than those of  $\text{NaSr}_4(\text{BO}_3)_3$  [5.15 eV,  $C_2$  point symmetry ( $\text{SrO}_8$ ) polyhedron with a mean bond length of 2.687 Å] and  $\text{Li}_6\text{Y}(\text{BO}_3)_3$  [5.01 eV,  $C_1$  point symmetry ( $\text{YO}_8$ ) polyhedron with an average bond distance of 2.376 Å].<sup>8,23,25,26</sup> The centroid energy is related to the nephelauxetic effect, the covalency between  $\text{O}^{2-}$  anions and  $\text{Ce}^{3+}$  cations, and/or the spectroscopic polarizability of  $\text{O}^{2-}$  anions in the first coordination sphere of  $\text{Ce}^{3+}$  cations. The comparisons presented above indicate that  $\text{Ce}^{3+}$  ions possess a moderate spectroscopic polarizability, covalency, and nephelauxetic effect in host compound  $\text{LiSr}_4(\text{BO}_3)_3$ .

In terms of the energy difference between the first 5d ( $5d_1$ ) and the fifth 5d ( $5d_5$ ) states in  $\text{Ce}^{3+}$  ions, the crystal field splitting energy ( $E_{\text{cfs}}$ ) is calculated to be  $\sim 2.27 \text{ eV}$  ( $18.3 \times 10^3 \text{ cm}^{-1}$ ), which is affected by the shape and size of the first anion coordination polyhedron around  $\text{Ce}^{3+}$  cations. Generally, the smaller coordination number and the shorter bond length will lead to a larger  $E_{\text{cfs}}$ . For the  $\text{Ce}^{3+}$  occupying six-coordinated sites in some host compounds, the  $E_{\text{cfs}}$  values are in the range of  $18.6 \times 10^3$  to  $23.3 \times 10^3 \text{ cm}^{-1}$  with an arithmetic average value of  $20.1 \times 10^3 \text{ cm}^{-1}$ , whereas for  $\text{Ce}^{3+}$  ions at eight-fold sites in some host compounds, the  $E_{\text{cfs}}$  values have been reported to be in the range from  $16.2 \times 10^3$  to  $19.6 \times 10^3 \text{ cm}^{-1}$  with a mean value of  $\sim 17.8 \times 10^3 \text{ cm}^{-1}$ .<sup>8,27</sup> The latter average value is closer to that in our case ( $18.1 \times 10^3 \text{ cm}^{-1}$ ), which implies that the spectral data we obtained above may relate to the  $\text{Ce}^{3+}$  ions in eight-fold coordinated  $C_2$  symmetry  $\text{Sr}^{2+}$  sites in  $\text{LiSr}_4(\text{BO}_3)_3$ .

The viewpoint described above can be further verified by the theoretical simulations of 4f– $5d_j$  ( $j = 1-5$ ) transitions of  $\text{Ce}^{3+}$  ions. Panels c and d of Figure 3 show the calculated 4f– $5d_j$  ( $j = 1-5$ ) transition energies of  $\text{Ce}^{3+}$  ions in  $\text{Sr}^{2+}$  sites when the CN of  $\text{Sr}^{2+}$  is eight and that of  $\text{LiSr}_4(\text{BO}_3)_3$  is six. The calculated and experimental results are also listed in Table 2 for comparison. It is obvious that the experimental excitation spectrum can be attributed to the 4f–5d transitions of  $\text{Ce}^{3+}$  ions in eight-coordinated  $\text{Sr}^{2+}$  sites, indicating that the  $\text{Ce}^{3+}$  ions preferentially occupy eight-coordinated rather than six-coordinated  $\text{Sr}^{2+}$  sites.

The calculation of the relative formation energy can provide an explanation for the preferential occupancy of  $\text{Ce}^{3+}$  in two  $\text{Sr}^{2+}$  sites. The formation energy of  $\text{Ce}^{3+}$  ions at  $[\text{Sr}(1)\text{O}_6]$  sites is higher than that at  $[\text{Sr}(2)\text{O}_8]$  sites by 0.51 eV, from which it is estimated that the concentration of the latter is higher than

**Table 2.** Calculated and Experimental 4f–5d<sub>*j*</sub> (*j* = 1–5) Transition Energies of Ce<sup>3+</sup> Ions

5d multiplet	calculated (eV)		experimental (eV)
	six-coordinated	eight-coordinated	
5d <sub>1</sub>	3.57	3.84	3.74
5d <sub>2</sub>	3.57	4.42	4.33
5d <sub>3</sub>	3.87	4.62	4.64
5d <sub>4</sub>	6.03	5.52	5.61
5d <sub>5</sub>	6.03	5.96	6.01

the former by >2 orders of magnitude, in agreement with the assignment determined from the excitation spectrum in Figure 3.

**3.4. Concentration-Dependent Luminescence of LiSr<sub>4</sub>(BO<sub>3</sub>)<sub>3</sub>:Ce<sup>3+</sup>.** The highest height-normalized excitation spectra of Li<sub>1+x</sub>Sr<sub>4-2x</sub>Ce<sub>x</sub>(BO<sub>3</sub>)<sub>3</sub> (*x* = 0.001, 0.005, 0.01, or 0.03) samples are shown in the left-hand inset of Figure 4. It

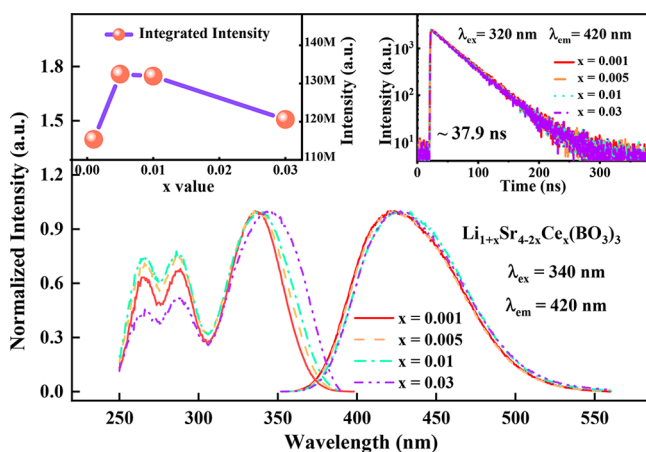


**Figure 4.** Highest height-normalized emission ( $\lambda_{\text{ex}} = 340$  nm) and excitation ( $\lambda_{\text{em}} = 420$  nm) spectra of Li<sub>1+x</sub>Sr<sub>4-2x</sub>Ce<sub>x</sub>(BO<sub>3</sub>)<sub>3</sub> (*x* = 0.001, 0.005, 0.01, or 0.03) at RT. The insets show the integrated intensity of emission spectra and the fluorescence decay curves ( $\lambda_{\text{ex}} = 320$  nm, and  $\lambda_{\text{em}} = 420$  nm) of Li<sub>1+x</sub>Sr<sub>4-2x</sub>Ce<sub>x</sub>(BO<sub>3</sub>)<sub>3</sub>.

can be found that the peak positions of the 4f–5d<sub>*j*</sub> (*j* = 2 or 3) excitation bands remain stable for samples with different doping concentrations, but that of the lowest 4f–5d excitation band gradually shifts to the long wavelength side. We assume that this phenomenon is mainly related to the slight increase in the 5d crystal field splitting (CFS) of Ce<sup>3+</sup> ions, as the smaller radius of Ce<sup>3+</sup> compared to that of Sr<sup>2+</sup> results in the contraction of the local coordination environment around Ce<sup>3+</sup> with increasing doping contents. The right-hand inset of Figure 4 displays the emission spectra of Li<sub>1+x</sub>Sr<sub>4-2x</sub>Ce<sub>x</sub>(BO<sub>3</sub>)<sub>3</sub> (*x* = 0.001, 0.005, 0.01, or 0.03) samples under 340 nm excitation. One can see that all spectral profiles are almost identical, but they slightly move in the long wavelength direction with an increase in Ce<sup>3+</sup> content, as a consequence of the larger CFS of the Ce<sup>3+</sup> 5d state at a higher doping level.

The inset in the top left corner of Figure 4 presents the integrated emission intensity in the range of 350–560 nm as a function of doping concentration, showing that the intensity increases first, reaches maximum at *x* = 0.005, and then decreases with an increase in concentration. Furthermore, the luminescence decay curves of Li<sub>1+x</sub>Sr<sub>4-2x</sub>Ce<sub>x</sub>(BO<sub>3</sub>)<sub>3</sub> (*x* = 0.001, 0.005, 0.01, or 0.03) all overlap as presented at the top right

corner of Figure 4, and they can be well fitted with an exponential function with a lifetime of ~37.9 ns. This value measured at RT is slightly smaller than that (~41.3 ns) collected at a low temperature of 78 K in Figure 2, due to thermal quenching as discussed in detail in Figure 6 (vide infra). Although the intensity-dependent luminescence and decay-dependent luminescence are somewhat inconsistent, the decay curves may provide better evidence because many experimental factors influence the spectral measurement results.<sup>28</sup> In other words, no concentration quenching occurs in the investigated doping contents.

Figure 2 has illustrated that the inhomogeneous broadening effect is not pronounced in the diluted Li<sub>1.001</sub>Sr<sub>3.998</sub>Ce<sub>0.001</sub>(BO<sub>3</sub>)<sub>3</sub> sample as mentioned in section 3.2. Further assessing the inhomogeneous broadening in a concentrated sample to gain insight into the influence of doping content on the inhomogeneous broadening effect is worthwhile. Therefore, the excitation and emission spectra as well as the luminescence decay curves of Li<sub>1.03</sub>Sr<sub>3.94</sub>Ce<sub>0.03</sub>(BO<sub>3</sub>)<sub>3</sub>, which has a Ce<sup>3+</sup> doping concentration 30 times higher than that of Li<sub>1.001</sub>Sr<sub>3.998</sub>Ce<sub>0.001</sub>(BO<sub>3</sub>)<sub>3</sub>, are shown in Figure 5. One can observe that the highest height-

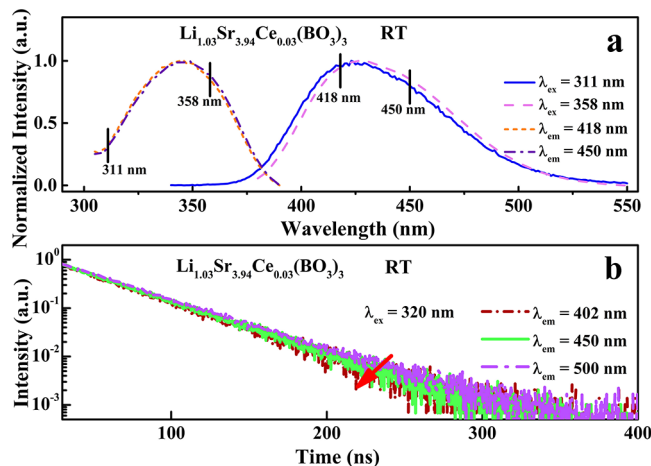


**Figure 5.** (a) Emission ( $\lambda_{\text{ex}} = 311$  and 358 nm) and excitation spectra ( $\lambda_{\text{em}} = 418$  and 450 nm) of Li<sub>1.03</sub>Sr<sub>3.94</sub>Ce<sub>0.03</sub>(BO<sub>3</sub>)<sub>3</sub> at RT. (b) Luminescence decay curves ( $\lambda_{\text{ex}} = 320$  nm, and  $\lambda_{\text{em}} = 402$ , 450, and 500 nm) of Li<sub>1.03</sub>Sr<sub>3.94</sub>Ce<sub>0.03</sub>(BO<sub>3</sub>)<sub>3</sub> at RT.

normalized first f–d excitation band (4f–5d<sub>1</sub>) is almost invariable when different emission wavelengths of 418 and 450 nm are monitored, but the emission band shifts slightly in the long wavelength direction as the excitation wavelength moves from the left side (311 nm) to the right side (358 nm) across the first f–d excitation peak (Figure 5a). One of the possible reasons for the observations may be that the inhomogeneous broadening effect is somewhat enhanced in this concentrated Li<sub>1.03</sub>Sr<sub>3.94</sub>Ce<sub>0.03</sub>(BO<sub>3</sub>)<sub>3</sub> sample in comparison to that in the diluted Li<sub>1.001</sub>Sr<sub>3.998</sub>Ce<sub>0.001</sub>(BO<sub>3</sub>)<sub>3</sub> sample.<sup>29,30</sup>

The existence of inhomogeneous broadening in this concentrated sample can be further corroborated by the fluorescence decay curves under 320 nm excitation and different wavelength emission. When the monitored emission wavelength shifts from 500 nm to 450 and 402 nm, the decay of Ce<sup>3+</sup> luminescence accelerates gradually and the lifetime is shorter steadily as shown in Figure 5b. The shorter the monitored emission wavelength, the faster the luminescence decay and the shorter the luminescence lifetime. There are

some unevenly distributed disturbed  $\text{Ce}^{3+}$  sites in the highly doping samples, and the  $4f-5d$  transition energies of these ions are slightly different, individually. The successive site-to-site energy transfer provides a channel for changing the luminescence lifetime; therefore, the decay time changes with detection wavelength across the emission band, and the luminescence decay curve deviates from the exponential form more or less.<sup>31–33</sup>

**3.5. Luminescence of  $\text{Li}_{1.001}\text{Sr}_{3.998}\text{Ce}_{0.001}(\text{BO}_3)_3$  at Different Temperatures.** Upon 335 nm excitation, the temperature-dependent emission spectra of the  $\text{Li}_{1.001}\text{Sr}_{3.998}\text{Ce}_{0.001}(\text{BO}_3)_3$  sample are measured in the range of 100–500 K as shown in Figure 6a. With an increase in

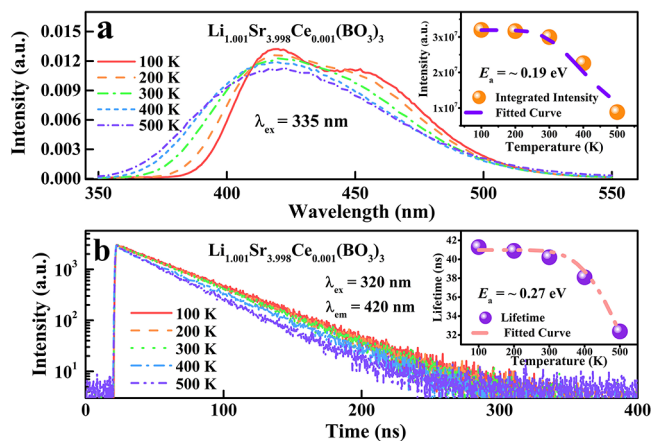


**Figure 6.** (a) Normalized emission spectra ( $\lambda_{\text{ex}} = 335$  nm) and (b) luminescence decay curves ( $\lambda_{\text{ex}} = 320$  nm, and  $\lambda_{\text{em}} = 420$  nm) of  $\text{Li}_{1.001}\text{Sr}_{3.998}\text{Ce}_{0.001}(\text{BO}_3)_3$  at 100–500 K. The insets show the integrated intensity or lifetime as a function of temperature and their fitting results using eqs 1 and 2, respectively.

temperature, the typical double emission peaks of  $\text{Ce}^{3+}$  ions gradually merged into a single peak gradually like normal cases. The inset shows that the integrated emission intensity remains almost stable below 300 K and then decreases with an increase in temperature, indicating that the thermal quenching of  $\text{Ce}^{3+}$  luminescence occurs in  $\text{LiSr}_4(\text{BO}_3)_3$ . The thermal quenching can be also confirmed by the temperature-dependent luminescence decay curves of the  $\text{Li}_{1.001}\text{Sr}_{3.998}\text{Ce}_{0.001}(\text{BO}_3)_3$  sample. As shown in Figure 6b, three fluorescence decay curves almost overlap with each other in the temperature range of 100–300 K. Then, the decay begins to accelerate above 300 K.

According to the temperature-dependent intensity or lifetime in the insets of Figure 6, the thermal quenching activation energy of  $\text{Ce}^{3+}$  f–d emission in  $\text{LiSr}_4(\text{BO}_3)_3$  can be evaluated by the single-barrier quenching model derived in eqs 1 and 2.

$$I(T) = \frac{I_0}{1 + \left(\frac{\Gamma_0}{\Gamma_v}\right) \exp[-E_{(a,I)}/kT]} \quad (1)$$

$$\tau(T) = \frac{\frac{1}{\Gamma_v}}{1 + \frac{\Gamma_0}{\Gamma_v} \exp[-E_{(a,\tau)}/kT]} \quad (2)$$

where  $I(T)$  and  $\tau(T)$  are the integrated emission intensity and lifetime at temperature  $T$ , respectively,  $\Gamma_0$  and  $\Gamma_v$  are the thermal quenching rate at  $T = \infty$  (attempt rate) and the

radiative  $\text{Ce}^{3+}$   $5d \rightarrow 4f$  transition rate, respectively,  $E_{(a,I)}$  and  $E_{(a,\tau)}$  represent the activation energies for thermal quenching of  $\text{Ce}^{3+}$  luminescence deduced by intensity and lifetime, respectively, and  $k$  is the Boltzmann constant ( $8.62 \times 10^{-5}$  eV  $\text{K}^{-1}$ ). Therefore, the values of  $E_{(a,I)}$  and  $E_{(a,\tau)}$  are simulated to be  $\sim 0.19$  and  $\sim 0.27$  eV, respectively, for this diluted  $\text{Li}_{1.001}\text{Sr}_{3.998}\text{Ce}_{0.001}(\text{BO}_3)_3$  sample.

The luminescence of  $4f-5d$  transitions of  $\text{Ce}^{3+}$  and/or  $\text{Eu}^{2+}$  ions may be thermally quenched by different nonradiative channels.<sup>28,34–37</sup> Three mechanisms were proposed to explain the thermal quenching characteristics of  $\text{Ce}^{3+}$ -doped phosphors.

Initially, the nonradiation  $5d \rightarrow 4f$  crossover relaxation via electron–phonon coupling is thought to be responsible for the thermal quenching of  $\text{Ce}^{3+}$  luminescence. In terms of this viewpoint, the activation energy of thermal quenching corresponds to the energy barrier ( $E_{\text{fd}}$ ) between the lowest point of the excited-state  $5d$  parabola and the intersection point of  $4f$  and  $5d$  parabolas in the configurational coordinate diagram. Accordingly, the energy barrier ( $E_{\text{fd}}$ ) in this case is estimated according to eq 3.<sup>35</sup>

$$E_{\text{fd}} = \frac{E_{\text{em}}^2}{4E_{\text{FC}}} \quad (3)$$

where  $E_{\text{em}}$  is the emission energy [2.99 eV (415 nm)] in our case and  $E_{\text{FC}}$  is the Franck–Condon shift (0.38 eV), which is approximately equal to half of the Stokes shift ( $\sim 0.75$  eV).<sup>38</sup> Therefore, the value of  $E_{\text{fd}}$  is 5.88 eV in the  $\text{Li}_{1.001}\text{Sr}_{3.998}\text{Ce}_{0.001}(\text{BO}_3)_3$  sample. Apparently, the crossing energy barrier is so large that the  $5d \rightarrow 4f$  crossover mechanism is unlikely to cause the thermal quenching of  $\text{Ce}^{3+}$  emission in the  $\text{LiSr}_4(\text{BO}_3)_3$  host compound.

Latterly, the thermal ionization of the  $5d$  electrons of  $\text{Ce}^{3+}$  ions into the conduction band of the host compound has been considered to be the channel resulting in the thermal quenching of  $\text{Ce}^{3+}$ . In this scenario, the activation energy of thermal quenching should be close to the energy barrier ( $E_{\text{dc}}$ ) between the lowest  $5d$  energy level of  $\text{Ce}^{3+}$  and the conduction band minimum of the host compound. To derive this energy barrier ( $E_{\text{dc}}$ ) in the  $\text{LiSr}_4(\text{BO}_3)_3$  host compound, the vacuum referred binding energy (VRBE) scheme is constructed as depicted in Figure 7.<sup>3</sup> The adopted experimental data for the construction include the bandgap energy ( $\sim 7.44$  eV) of  $\text{LiSr}_4(\text{BO}_3)_3$ , the energies (3.74, 4.33, 4.64, 5.61, and 6.01 eV) of the  $\text{Ce}^{3+}$   $4f-5d$  transitions, and the exchange splitting energy (0.84 eV) of  $\text{Tb}^{3+}$  electron transitions between the low spin and high spin in the  $\text{LiSr}_4(\text{BO}_3)_3$  host as displayed in Figure S2. The additional empirical datum involves a Coulomb interaction  $U_c$  value of 6.89 eV, which corresponds to the energy difference between the  $4f$  ground states of  $\text{Eu}^{2+}$  and  $\text{Eu}^{3+}$  ions and calculated from the chemical shift model.<sup>3</sup> The VRBE scheme reveals the  $E_{\text{dc}}$  value of  $\text{Ce}^{3+}$  is 0.29 eV, which is near the experimental fitting values ( $\sim 0.19$  and 0.27 eV, with a mean value of  $0.23 \pm 0.04$  eV) from the temperature-dependent intensity or lifetime in the insets of Figure 7. Several factors such as the relaxation of the  $4f-5d$  transition, the construction of the VRBE scheme, the fitting of the thermal quenching activation energy, etc., would impose influences on this difference. Regardless, the values are enough to explain the thermal quenching mechanism we developed here. Hence, we assume that the electron thermal-ionization process provides an important channel for  $\text{Ce}^{3+}$  thermal quenching in



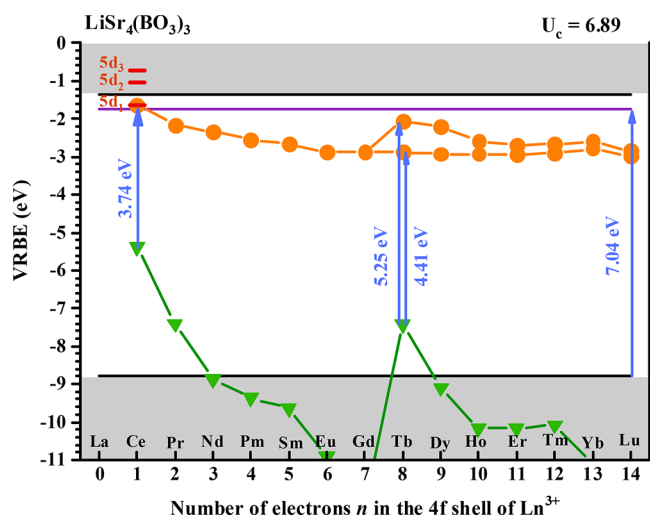


**Figure 7.** Vacuum referred binding energy (VRBE) scheme of trivalent lanthanide ions in  $\text{LiSr}_4(\text{BO}_3)_3$ . The top and bottom black solid lines are the conduction band minimum (CBM) and the valence band maximum (VBM), respectively. The distance between the purple line and the top black solid line corresponds to the electron–hole binding energy. The green triangles and orange circles represent the lowest 5d states and 4f ground states of  $\text{Ln}^{3+}$ , respectively.

$\text{Li}_{1.001}\text{Sr}_{3.998}\text{Ce}_{0.001}(\text{BO}_3)_3$ . In addition, the thermally activated concentration quenching may also contribute to the thermal quenching. In this process, nonradiative energy migration happens among doping luminescence centers and finally to killer centers like oxygen vacancies or holes in materials<sup>28,35,37</sup> with an increase in temperature, closely related to the resonance energy transfer process.<sup>39</sup> With an increase in doping concentration, the spectral overlap between the excitation band and emission band usually increases. Consequently, the energy transfer probability between doping ions and that to the quenching centers increases, which eventually results in a decrease in the thermal quenching temperature and the thermal quenching activation energy.

To assess the influence of this factor on the thermal quenching, the temperature-dependent emission spectra and luminescence decay curves of a concentrated  $\text{Li}_{1.03}\text{Sr}_{3.94}\text{Ce}_{0.03}(\text{BO}_3)_3$  sample are measured at 100–500 K as shown in Figure S3. The fitted values of  $E_{(a,l)}$  and  $E_{(a,r)}$  are  $\sim 0.15$  and  $\sim 0.18$  eV, respectively. The values are slightly smaller than the corresponding values of the diluted  $\text{Li}_{1.001}\text{Sr}_{3.998}\text{Ce}_{0.001}(\text{BO}_3)_3$  sample. It seems that the thermally activated concentration quenching partially contributes to the thermal quenching of the luminescence of  $\text{Ce}^{3+}$  in  $\text{LiSr}_4(\text{BO}_3)_3$ .

**3.6. X-ray Excited Luminescence of  $\text{Li}_{1.01}\text{Sr}_{3.98}\text{Ce}_{0.01}(\text{BO}_3)_3$ .** The X-ray excitation luminescence (XEL) measurement of the  $\text{Li}_{1.01}\text{Sr}_{3.98}\text{Ce}_{0.01}(\text{BO}_3)_3$  sample is performed to evaluate the potential detecting application. The XEL spectra of the  $\text{Li}_{1.01}\text{Sr}_{3.98}\text{Ce}_{0.01}(\text{BO}_3)_3$  compound and  $\text{BaF}_2$  reference single crystal at RT are shown in Figure 8. The emission spectrum of the  $\text{Li}_{1.01}\text{Sr}_{3.98}\text{Ce}_{0.01}(\text{BO}_3)_3$  sample exhibits a broad band in the range of 350–550 nm, which is consistent with that under UV light excitation. The emission curve of a  $\text{BaF}_2$  reference single crystal is in agreement with that in ref 14. Upon calculation of the ratio of the integrated intensity of two samples, the photon yield of the  $\text{Li}_{1.01}\text{Sr}_{3.98}\text{Ce}_{0.01}(\text{BO}_3)_3$  sample is estimated to be  $\sim 12.0 \times$

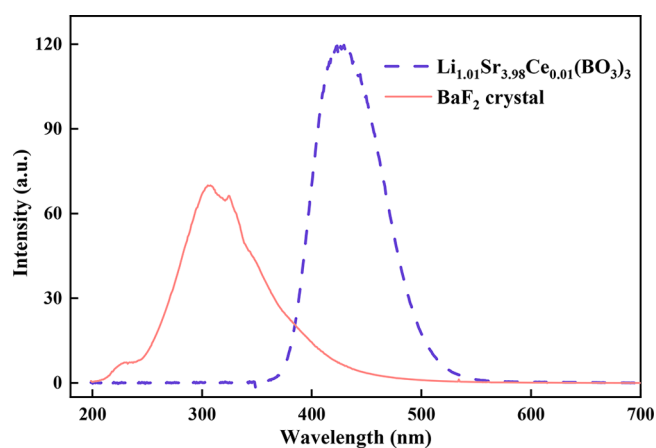


**Figure 8.** X-ray excited luminescence (XEL) spectra of the  $\text{BaF}_2$  crystal and the  $\text{Li}_{1.01}\text{Sr}_{3.98}\text{Ce}_{0.01}(\text{BO}_3)_3$  sample at RT.

$10^3$  photons/MeV using the photon yield of 8800 photons/MeV of the  $\text{BaF}_2$  reference crystal. This value is also higher than that of commercial  $\text{Bi}_4\text{Ge}_3\text{O}_{12}$  powder (8200 photons/MeV).<sup>40</sup> The  $\text{Li}_{1.01}\text{Sr}_{3.98}\text{Ce}_{0.01}(\text{BO}_3)_3$  powder is worth further optimization as a potential X-ray detecting material.

#### 4. CONCLUSIONS

In this paper, the site occupancy, VUV–UV–vis photoluminescence, and X-ray radio-luminescence of  $\text{Ce}^{3+}$  ions doped in  $\text{LiSr}_4(\text{BO}_3)_3$  are systematically studied, after the sample preparation by a traditional high-temperature solid-state reaction approach and the phase purity and structure characterization by the high-resolution XRD Rietveld refinement. First, the bandgap energy of the host compound is estimated to be  $\sim 7.44$  eV according to the synchrotron radiation VUV–UV excitation spectra of  $\text{Ce}^{3+}$ - and  $\text{Gd}^{3+}$ -doped  $\text{LiSr}_4(\text{BO}_3)_3$ . In addition, the excitation bands of  $\text{Ce}^{3+}$  ions in  $\text{LiSr}_4(\text{BO}_3)_3$  are observed around 331, 286, 267, 221, and 206 nm and attributed to the transitions to the five 5d crystal field states of  $\text{Ce}^{3+}$  ions located at the eight-fold coordinated  $\text{Sr}^{2+}$  sites with  $C_2$  symmetry, not those six-fold coordinated sites. Second, the preferential occupancy of  $\text{Ce}^{3+}$  ions is further confirmed by the calculated 4f–5d ( $j = 1-5$ ) transition energies of  $\text{Ce}^{3+}$  ions located at both of two sites in the first-principles framework, as there is good agreement between the experimental results and the calculated ones for the eight-fold coordinated case ( $31.0 \times 10^3$ ,  $35.7 \times 10^3$ ,  $37.3 \times 10^3$ ,  $44.5 \times 10^3$ , and  $48.1 \times 10^3 \text{ cm}^{-1}$ ), and a large mismatch with the six-fold coordinated case ( $28.8 \times 10^3$ ,  $28.8 \times 10^3$ ,  $31.2 \times 10^3$ ,  $48.6 \times 10^3$ , and  $48.6 \times 10^3 \text{ cm}^{-1}$ ). Moreover, the preferential occupancy can be explained by the calculated relative defect formation energies (0.51 and 0.00 eV) of  $\text{Ce}^{3+}$  located at  $[\text{Sr}(1)\text{O}_6]$  and  $[\text{Sr}(2)\text{O}_8]$  sites, respectively. Third, the doping concentration-dependent luminescence and temperature-dependent luminescence are investigated by the luminescence spectra and decay curves, respectively. There is no concentration quenching for the studied doping concentration range, but the inhomogeneous broadening effect is observed. Upon systematic analysis of the thermal quenching activation energies fitted from the experimental spectroscopic data using three kinds of thermal quenching mechanism models, the thermal-ionization mechanism from the 5d states to the host's conduction band bottom is thought to be predominately responsible for the observed thermal quenching

effect, although the potential contribution of the thermally activated concentration quenching is not completely ignored. Finally, the photon yield of  $\sim 12.0 \times 10^3$  photons/MeV of the  $\text{Li}_{1.01}\text{Sr}_{3.98}\text{Ce}_{0.01}(\text{BO}_3)_3$  sample estimated from XEL measurement demonstrates its potential applications in X-ray detection.

## ■ ASSOCIATED CONTENT

### SI Supporting Information

The Supporting Information is available free of charge at <https://pubs.acs.org/doi/10.1021/acs.inorgchem.2c01016>.

VUV–UV excitation and emission spectra of  $\text{Li}_{1.001}\text{Sr}_{3.998}\text{Gd}_{0.001}(\text{BO}_3)_3$ , VUV excitation spectrum of  $\text{Li}_{1.001}\text{Sr}_{3.998}\text{Tb}_{0.001}(\text{BO}_3)_3$  at 11 K, normalized emission spectra and luminescence decay curves of a concentrated  $\text{Li}_{1.03}\text{Sr}_{3.94}\text{Ce}_{0.03}(\text{BO}_3)_3$  sample at 100–500 K, and fitting results of the integrated intensity and lifetime as a function of temperature (PDF)

## ■ AUTHOR INFORMATION

### Corresponding Author

Hongbin Liang – MOE Key Laboratory of Bioinorganic and Synthetic Chemistry, KLGHEI of Environment and Energy Chemistry, School of Chemistry, Sun Yat-sen University, Guangzhou 510006, China; [orcid.org/0000-0002-3972-2049](https://orcid.org/0000-0002-3972-2049); Email: [cesbin@mail.sysu.edu.cn](mailto:cesbin@mail.sysu.edu.cn)

### Authors

Yunlin Yang – MOE Key Laboratory of Bioinorganic and Synthetic Chemistry, KLGHEI of Environment and Energy Chemistry, School of Chemistry, Sun Yat-sen University, Guangzhou 510006, China

Bibo Lou – CAS Key Laboratory of Microscale Magnetic Resonance and School of Physical Sciences, University of Science and Technology of China, Hefei 230026, China

Yiyi Ou – MOE Key Laboratory of Bioinorganic and Synthetic Chemistry, KLGHEI of Environment and Energy Chemistry, School of Chemistry, Sun Yat-sen University, Guangzhou 510006, China; [orcid.org/0000-0002-2111-5064](https://orcid.org/0000-0002-2111-5064)

Fang Su – MOE Key Laboratory of Bioinorganic and Synthetic Chemistry, KLGHEI of Environment and Energy Chemistry, School of Chemistry, Sun Yat-sen University, Guangzhou 510006, China

Chong-Geng Ma – School of Optoelectronic Engineering and CQUPT-BUL Innovation Institute, Chongqing University of Posts and Telecommunications, Chongqing 400065, China

Chang-Kui Duan – CAS Key Laboratory of Microscale Magnetic Resonance and School of Physical Sciences, University of Science and Technology of China, Hefei 230026, China; [orcid.org/0000-0003-1016-4976](https://orcid.org/0000-0003-1016-4976)

Pieter Dorenbos – Faculty of Applied Sciences, Delft University of Technology, 2629 JB Delft, The Netherlands

Complete contact information is available at:

<https://pubs.acs.org/doi/10.1021/acs.inorgchem.2c01016>

### Notes

The authors declare no competing financial interest.

## ■ ACKNOWLEDGMENTS

This work was financially supported by the National Natural Science Foundation of China (Grants 22171290, 52161135110, and 11974338), the National Key Research

and Development Program of China (Grant 2018YFA0306600), the China-Poland Intergovernmental Science and Technology Cooperation Program (2020[15]/10), and the Natural Science Foundation of Guangdong Province (2022A1515011376). The measurements on the vacuum ultraviolet (VUV) spectra of the samples were carried out with the support of the 4B8 beamline at the Beijing Synchrotron Radiation Facility (BSRF).

## ■ REFERENCES

- (1) Yen, W. M.; Shionoya, S.; Yamamoto, H. *Phosphor Handbook*, 2nd ed.; CRC Press: Boca Raton, FL, 2006.
- (2) Qin, X.; Liu, X.; Huang, W.; Bettinelli, M.; Liu, X. Lanthanide-Activated Phosphors Based on 4f-5d Optical Transitions: Theoretical and Experimental Aspects. *Chem. Rev.* **2017**, *117*, 4488–4527.
- (3) Dorenbos, P. Improved parameters for the lanthanide 4f<sup>n</sup> and 4f<sup>n-1</sup>5d curves in HRBE and VRBE schemes that takes the nephelauxetic effect into account. *J. Lumin.* **2020**, *222*, 117164.
- (4) Dorenbos, P. Fundamental Limitations in the Performance of Ce<sup>3+</sup>, Pr<sup>3+</sup>, and Eu<sup>2+</sup>-Activated Scintillators. *IEEE Trans. Nucl. Sci.* **2010**, *57*, 1162–1167.
- (5) Xie, M.; Wei, H.; Wu, W. Site Occupancy Studies and Luminescence Properties of Emission Tunable Phosphors Ca<sub>9</sub>La(PO<sub>4</sub>)<sub>7</sub>:Re (Re = Ce<sup>3+</sup>, Eu<sup>2+</sup>). *Inorg. Chem.* **2019**, *58*, 1877–1885.
- (6) Tong, X.; Han, J.; Cai, R.; Xu, Y.; Wu, P.; Zhou, H.; Zhang, X. Multisite-Occupancy-Driven Efficient Multiple Energy Transfer: A Straightforward Strategy to Achieve Single-Composition White-Light Emission in Ce<sup>3+</sup>, Tb<sup>3+</sup>, and Mn<sup>2+</sup>-Doped Silicate Phosphors. *Inorg. Chem.* **2020**, *59*, 9838–9846.
- (7) Fan, P.; Xu, Z.; Luo, Q.; He, Z.; Chen, Y.; Miao, Q.; Huang, C.; Liu, X.; Li, L. Theoretical Calculation of Bond Energy, Self-Reduction Phenomenon, and Photoluminescence Properties of Eu/Ce Single-Doped and Codoped Ba<sub>2</sub>CaB<sub>2</sub>Si<sub>4</sub>O<sub>14</sub> Phosphors. *J. Phys. Chem. C* **2021**, *125*, 17820–17830.
- (8) Dorenbos, P. 5d-level energies of Ce<sup>3+</sup> and the crystalline environment. III. Oxides containing ionic complexes. *Phys. Rev. B* **2001**, *64*, 125117–125118.
- (9) Zhou, W.; Pan, F.; Zhou, L.; Hou, D.; Huang, Y.; Tao, Y.; Liang, H. Site Occupancies, Luminescence, and Thermometric Properties of LiY<sub>9</sub>(SiO<sub>4</sub>)<sub>6</sub>O<sub>2</sub>:Ce<sup>3+</sup> Phosphors. *Inorg. Chem.* **2016**, *55*, 10415–10424.
- (10) Wen, J.; Wang, Y.; Jiang, G.; Zhong, J.; Chu, J.; Xia, Q.; Zhang, Q.; Ning, L.; Duan, C.-K.; Yin, M. First-Principles Study on Self-Activated Luminescence and 4f → 5d Transitions of Ce<sup>3+</sup> in M<sub>5</sub>(PO<sub>4</sub>)<sub>3</sub>X (M = Sr, Ba; X = Cl, Br). *Inorg. Chem.* **2020**, *59*, 5170–5181.
- (11) Jing, W.; Liu, M.; Wen, J.; Ning, L.; Yin, M.; Duan, C.-K. First-principles study of Ti-doped sapphire. II. Formation and reduction of complex defects. *Phys. Rev. B* **2021**, *104*, 165104.
- (12) Wu, L.; Chen, X. L.; Li, H.; He, M.; Xu, Y. P.; Li, X. Z. Structure Determination and Relative Properties of Novel Cubic Borates MM'<sub>4</sub>(BO<sub>3</sub>)<sub>3</sub> (M = Li, M' = Sr; M = Na, M' = Sr, Ba). *Inorg. Chem.* **2005**, *44*, 6409–6414.
- (13) Coelho, A. A. *TOPAS Academic*, ver. 4; Coelho Software: Brisbane, Australia, 2005.
- (14) Zhou, R.; Ma, F.; Su, F.; Ou, Y.; Qi, Z.; Zhang, J.; Huang, Y.; Dorenbos, P.; Liang, H. Site occupancies, VUV-UV-vis photoluminescence and X-ray radioluminescence of Eu<sup>2+</sup> doped RbBaPO<sub>4</sub>. *Inorg. Chem.* **2020**, *59*, 17421–17429.
- (15) Perdew, J. P.; Burke, K.; Ernzerhof, M. Generalized gradient approximation made simple. *Phys. Rev. Lett.* **1996**, *77*, 3865–3868.
- (16) Cai, J.; Jing, W.; Cheng, J.; Zhang, Y.; Chen, Y.; Yin, M.; Yeung, Y.-Y.; Duan, C.-K. First-principles calculations of photoluminescence and defect states of Ce<sup>3+</sup>-doped (Ca/Sr)<sub>2</sub>B<sub>5</sub>O<sub>9</sub>Cl. *Phys. Rev. B* **2019**, *99*, 125107.
- (17) Momma, K.; Izumi, F. VESTA 3 for three-dimensional visualization of crystal, volumetric and morphology data. *J. Appl. Crystallogr.* **2011**, *44*, 1272–1276.

- (18) Shannon, R. D. Revised Effective Ionic Radii and Systematic Studies of Interatomic Distances in Halides and Chalcogenides. *Acta Crystallogr.* **1976**, *A32*, 751–767.
- (19) Setlur, A. A.; Srivastava, A. M. On the relationship between emission color and  $\text{Ce}^{3+}$  concentration in garnet phosphors. *Opt. Mater.* **2007**, *29*, 1647–1652.
- (20) Zhang, X.; Lang, H.; Seo, H. J. On the luminescence of  $\text{Ce}^{3+}$ ,  $\text{Eu}^{3+}$ , and  $\text{Tb}^{3+}$  in Novel Borate  $\text{LiSr}_4(\text{BO}_3)_3$ . *J. Fluoresc.* **2011**, *21*, 1111–1115.
- (21) Guo, C.; Ding, X.; Seo, H. J.; Ren, Z.; Bai, J. Luminescent properties of UV excitable blue emitting phosphors  $\text{MSr}_4(\text{BO}_3)_3:\text{Ce}^{3+}$  ( $M = \text{Li}$  and  $\text{Na}$ ). *J. Alloys Compd.* **2011**, *509*, 4871–4874.
- (22) Wang, Q.; Deng, D.; Hua, Y.; Huang, L.; Wang, H.; Zhao, S.; Jia, G.; Li, C.; Xu, S. Potential tunable white-emitting phosphor  $\text{LiSr}_4(\text{BO}_3)_3:\text{Ce}^{3+}, \text{Eu}^{2+}$  for ultraviolet light-emitting diodes. *J. Lumin.* **2012**, *132*, 434–438.
- (23) Ding, X.; Liang, H.; Hou, D.; Jia, S.; Su, Q.; Sun, S.; Tao, Y. Site occupancy and luminescence of  $\text{Ce}^{3+}$  in  $\text{NaSr}_4(\text{BO}_3)_3$ . *J. Phys. D: Appl. Phys.* **2012**, *45*, 365301.
- (24) Dorenbos, P. Charge transfer bands in optical materials and related defect level location. *Opt. Mater.* **2017**, *69*, 8–22.
- (25) Zhou, W.; Hou, D.; Pan, F.; Zhang, B.; Dorenbos, P.; Huang, Y.; Tao, Y.; Liang, H. VUV-vis photoluminescence, X-ray radioluminescence and energy transfer dynamics of  $\text{Ce}^{3+}$  and  $\text{Pr}^{3+}$  doped  $\text{LiCaBO}_3$ . *J. Mater. Chem. C* **2015**, *3*, 9161–9169.
- (26) Ou, Y.; Zhou, W.; Hou, D.; Brik, M. G.; Dorenbos, P.; Huang, Y.; Liang, H. Impacts of 5d electron binding energy and electron-phonon coupling on luminescence of  $\text{Ce}^{3+}$  in  $\text{Li}_6\text{Y}(\text{BO}_3)_3$ . *RSC Adv.* **2019**, *9*, 7908–7915.
- (27) Aloui-Lebbou, O.; Goutaudier, C.; Kubota, S.; Dujardin, C.; Cohen-Adad, M. T.; Pédrini, C.; Florian, P.; Massiot, D. Structural and scintillation properties of new  $\text{Ce}^{3+}$ -doped alumino-borate. *Opt. Mater.* **2001**, *16*, 77–86.
- (28) Bachmann, V.; Ronda, C.; Meijerink, A. Temperature Quenching of Yellow  $\text{Ce}^{3+}$  Luminescence in YAG:Ce. *Chem. Mater.* **2009**, *21*, 2077–2084.
- (29) Kodama, N.; Yamaga, M.; Henderson, B. Inhomogeneous broadening of the  $\text{Ce}^{3+}$  luminescence in  $\text{CaYAlO}_4$ . *J. Phys.: Condens. Matter* **1996**, *8*, 3505–3512.
- (30) Yamaga, M.; Imai, T.; Miyairi, H.; Kodama, N. Substitutional disorder and optical spectroscopy of  $\text{Ce}^{3+}$ -doped  $\text{CaNaYF}_6$  crystals. *J. Phys.: Condens. Matter* **2001**, *13*, 753–764.
- (31) Lee, S.; Sohn, K.-S. Effect of inhomogeneous broadening on time-resolved photoluminescence in  $\text{CaAlSiN}_3:\text{Eu}^{2+}$ . *Opt. Lett.* **2010**, *35*, 1004–1006.
- (32) Duan, C.-K.; Tanner, P. A.; Makhov, V.; Khaidukov, N. Emission and Excitation Spectra of  $\text{Ce}^{3+}$  and  $\text{Pr}^{3+}$  Ions in Hexafluoroelpasolite Lattices. *J. Phys. Chem. A* **2011**, *115*, 8870–8876.
- (33) Leño, J. L.; Lesniewski, T.; Lazarowska, A.; Mahlik, S.; Grinberg, M.; Sheu, H.-S.; Liu, R.-S. Thermal Stabilization and Energy Transfer in Narrow-band Red-emitting  $\text{Sr}[(\text{Mg}_2\text{Al}_2)_{1-y}(\text{Li}_2\text{Si}_2)_y\text{N}_4]:\text{Eu}^{2+}$  Phosphors. *J. Mater. Chem. C* **2018**, *6*, 5975–5983.
- (34) Dorenbos, P. Thermal quenching of  $\text{Eu}^{2+}$  5d-4f luminescence in inorganic compounds. *J. Phys.: Condens. Matter* **2005**, *17*, 8103–8111.
- (35) Jia, Y.; Miglio, A.; Poncé, S.; Mikami, M.; Gonze, X. First-principles study of the luminescence of  $\text{Eu}^{2+}$ -doped phosphors. *Phys. Rev. B* **2017**, *96*, 125132.
- (36) Lin, Y.-C.; Bettinelli, M.; Karlsson, M. Unraveling the mechanisms of thermal quenching of luminescence in  $\text{Ce}^{3+}$ -doped garnet phosphors. *Chem. Mater.* **2019**, *31*, 3851–3862.
- (37) Linderlav, C.; Aberg, D.; Erhart, P. Luminescence quenching via deep defect states: A recombination pathway via oxygen vacancies in Ce-doped YAG. *Chem. Mater.* **2021**, *33*, 73–80.
- (38) Alkauskas, A.; McCluskey, M. D.; Van de Walle, C. G. Tutorial: Defects in semiconductors—Combining experiment and theory. *J. Appl. Phys.* **2016**, *119*, 181101.
- (39) Di Bartolo, B. *Advances in Nonradiative Processes in Solids*; Springer: New York, 1991.
- (40) Weber, M. J. Inorganic scintillators: today and tomorrow. *J. Lumin.* **2002**, *100*, 35–45.